Monitoring the crystal structure and the electrochemical properties of Na3(VO)2(PO4)2F through Fe3+ substitution

Long H. B. Nguyen, Jacob Olchowka, Stéphanie Belin, Paula Sanz Camacho, Mathieu Duttine, Antonella Iadecola, François Fauth, Dany Carlier, Christian Masquelier, Laurence Croguennec

Monitoring the Crystal Structure and the Electrochemical Properties of $Na_3(VO)_2(PO_4)_2F$ through Fe^{3+}-Substitution

Long H.B. Nguyen [a,b,e], Jacob Olchowka [a,e,f], Stéphanie Belin [c], Paula Sanz Camacho [a], Mathieu Duttine [a], Antonella Iadecola [e], François Fauth [d], Dany Carlier [a,e,f], Christian Masquelier [b,e,f], Laurence Croguennec [a,e,f] *

[a] CNRS, Univ. Bordeaux, Bordeaux INP, ICMCB UMR 5026, F-33600, Pessac, France.

[b] Laboratoire de Réactivité et de Chimie des Solides, CNRS-UMR #7314, Université de Picardie Jules Verne, F-80039 Amiens Cedex 1, France.

[c] SOLEIL Synchrotron, F-91192 Gif-sur-Yvette, France.

[d] CELLS-ALBA synchrotron, E-08290 Cerdanyola del Vallès, Barcelona, Spain.

[e] RS2E, Réseau Français sur le Stockage Electrochimique de l'Energie, FR CNRS 3459, F-80039 Amiens Cedex 1, France.

[f] ALISTORE-ERI European Research Institute, FR CNRS 3104, Amiens, F-80039 Cedex 1, France.

Key words: $Na_3V_2(PO_4)_2F_3$, $Na_3(VO)_2(PO_4)_2F$, Fe^{3+}-substitution, sodium-ion batteries, sol-gel synthesis, synchrotron X-ray diffraction, solid-state NMR, Na^+ diffusivity.

* Corresponding author: L. Croguennec (Laurence.Croguennec@icmcb.cnrs.fr)

Abstract

We here present the synthesis of a new material, $Na_3(VO)Fe(PO_4)_2F_2$, by sol-gel method. Its atomic and electronic structural description are determined by a combination of several diffraction and spectroscopy techniques, such as: synchrotron X-ray powder diffraction, synchrotron X-ray absorption spectroscopy at V and Fe K-edges, ^{57}Fe Mössbauer and ^{31}P solid-state nuclear magnetic resonance spectroscopy. The crystal structure of this newly obtained phase is similar to that of $Na_3(VO)_2(PO_4)_2F$, with a random distribution of Fe^{3+} ions over vanadium sites. Even though Fe^{3+} and V^{4+} ions situate on the same crystallographic position, their local environment can be studied separately by the use of ^{57}Fe Mössbauer and X-ray absorption spectroscopy at Fe and V K-edges, respectively. The Fe^{3+} ion resides in a symmetric octahedral environment while the octahedral site of V^{4+} is greatly distorted due to the presence of the vanadyl bond. No electrochemical activity of the Fe^{4+}/Fe^{3+} redox couple is detected, at least up to 5 V, whereas the reduction of Fe^{3+} into Fe^{2+} has been observed at ~ 1.5 V vs. Na^+/Na through the insertion of 0.5 Na^+ into $Na_3(VO)Fe(PO_4)_2F_2$. Comparing to $Na_3(VO)_2(PO_4)_2F$, the electrochemical profile of $Na_3(VO)Fe(PO_4)_2F_2$ in the same cycling condition shows a smaller polarization which could be due to a slight improvement in Na^+ diffusion process thanks to the presence of Fe^{3+} in the framework. Furthermore, the de-sodiation mechanism occurring upon charging is investigated by *operando* synchrotron X-ray diffraction and *operando* synchrotron X-ray absorption at V K-edge.

1. Introduction

Lithium-ion batteries (LIBs) have long been the dominant means of energy storage used for mobile devices thanks to their high operating voltage and high energy density. Nevertheless, the unequal presence of Li resources in the earth's crust and the increasing price of lithium precursors have motivated the development of alternative technologies in order to diversify the choice of energy storage systems. The revival of Sodium-ion batteries (SIBs) in the last decade has attracted great attention from the scientific community as the ubiquity of sodium resources widespread over the world would reduce the fabrication expense in case of large-scale production.[1–4] Recently, great progress has been made in the field of SIBs thanks to the similarity to their LIBs counterpart. Several layered and polyanionic compounds have already been extensively studied as positive electrode materials for SIBs: layered oxides with the general formula Na_xMO_2 (M = Transition metal), whose structure depends on the Na-content and the nature of the transition metal M, the fluorinated oxyphosphate $Na_3V_2(PO_4)_2F_3$ and $Na_3(VO)_2(PO_4)_2F$, or the NASICON-type compositions $Na_3V^{3+}{}_2(PO_4)_3$ and $Na_4V^{3+}Mn^{2+}(PO_4)_3$.[5,6,15,7–14]

Among all the polyanionic materials, the series of $Na_3V_{2-y}(VO)_y(PO_4)_2F_{3-y}$ ($0 \leq y \leq 2$) compositions is one of the most promising due to its high operating voltage, high reversible capacity and excellent stability upon long-term cycling.[6,16–18] Furthermore, the stability and the flexibility of their 3D structural framework allow their electrochemical and chemical properties to be tuned via cationic and/or anionic substitutions. The structure of $Na_3V_2(PO_4)_2F_3$ ($y = 0$) is described in **Figure 1**.

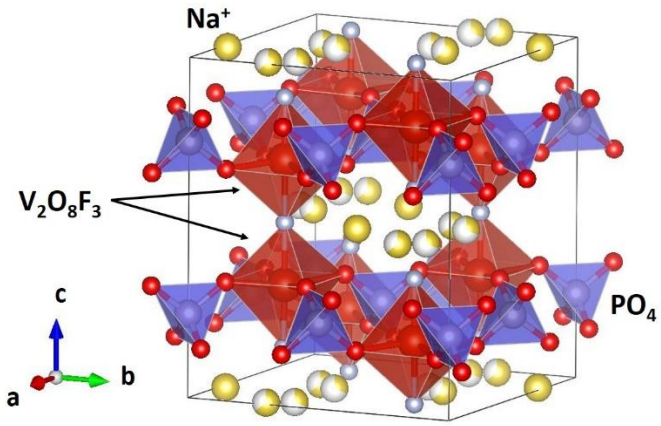

Figure 1 : The 3D crystal structure of $Na_3V_2(PO_4)_2F_3$. The bi-octahedral units $V_2O_8F_3$ and the tetrahedral PO_4 groups are shown as red and violet polyhedra, respectively. The Na^+ ions, represented by yellow balls, occupy the empty space in the structure at the crystallographic planes z = 0 and z = ½.

The relatively mobile Na^+ ions localized in the tunnels of the $Na_3V_2(PO_4)_2F_3$ type structure can be replaced easily by other monovalent cations, which results in Li^+, K^+ or Ag^+ ionic conductors.[19–22] The F/O anionic substitution can be performed on the terminal fluorine positions of the $V_2O_8F_3$ bi-octahedral units in $Na_3V_2(PO_4)_2F_3$, leading to a controlled formation of $Na_3V_{2-y}(VO)_y(PO_4)_2F_{3-y}$ ($0 \leq y \leq 2$) fluorinated oxyphosphate series.[6,23,24] Several examples of cationic substitution for vanadium have also been reported in the literature. For instance, Bianchini *et al*. succeeded to obtain a limited solid solution of $Na_3V_{2-z}Al_z(PO_4)_2F_3$ ($0 \leq z \leq 0.3$) by solid-state synthesis. Unfortunately, the polarization upon electrochemical cycling increases slightly for these Al-substituted phases.[21] Furthermore, the capacity loss observed in these compounds was considered as a detrimental effect of Al-substitution for V since only the V^{4+}/V^{3+} redox couple can be activated in the electrochemical window of all the currently available electrolytes.[25,26] A decrease in the charge transfer resistance and an improvement in the capacity retention were reported when $Na_3V_2(PO_4)_2F_3$ was doped with yttrium or manganese ions.[27,28] Nonetheless, there is no report on the effects of cationic substitution on the electrochemical performance of $Na_3(VO)_2(PO_4)_2F$ that can be found in the literature. In the frame of a prospective research in order to replace the critical element V by a sustainable one

and to study the electrochemical properties of cationic-substituted $Na_3(VO)_2(PO_4)_2F$ phases, we here synthesized the Fe^{3+}-substituted $Na_3(VO)_2(PO_4)_2F$ and investigated the crystal structure and electrochemical performance of this newly obtained phase by a combination of several characterization techniques.

2. Experimental methods

Material preparation. $Na_3(VO)Fe(PO_4)_2F_2$ was obtained through a sol-gel approach inspired by the work of Qi *et al*.[29] by using NaF (Sigma-Aldrich; ≥ 99%), $V(C_5H_7O_2)_3$ (Sigma-Aldrich; ≥ 97%), $Fe(NO_3)_3.9H_2O$ (Sigma-Aldrich; ≥ 98%), and $NH_4H_2PO_4$ (Sigma-Aldrich; ≥ 99.99%) precursors. The initial solution containing a mixture of NaF, $V(C_5H_7O_2)_3$, $Fe(NO_3)_3.9H_2O$, and $NH_4H_2PO_4$, dissolved in 5 mL of Ethanol and 3 mL of Acetone, is dark red due to the dark color of $V(C_5H_7O_2)_3$. The solution was prepared for the synthesis of 2 g of final product. After a few hours under stirring in a closed vessel, the solution turned into a deep blue color as V^{3+} ions present in the solution were gradually oxidized into V^{4+} by oxygen in air. After two days under continuous stirring, the cap was opened in order to evaporate the solvent at ambient temperature, which leads to the formation of a yellow viscous gel. This gel was placed into a golden crucible and first annealed at 150ºC during 3h to remove all the traces of solvent and then at 300ºC during 3h in order to decompose all the nitrate and ammonium-containing sources. Afterwards, the resulting powder was finely ground in a mortar, pelletized, and finally calcined at 550ºC during 3h under Ar atmosphere.

Structural characterization. Laboratory X-ray powder diffraction (XRD) patterns were obtained using a PANalytical Empyrean diffractometer equipped with a Cu K_α X-ray source. The data were recorded from 8°-80° with a step size of 0.0167°. High angular resolution synchrotron X-ray powder diffraction (SXRD) was performed at the MSPD beamline at ALBA (Barcelona, Spain) at the wavelength of 0.8251 Å, in the angular range 1^o - 64^o with a step size

of 0.006º. FullProf Suite and Jana 2006 softwares were used to perform Rietveld refinements on the obtained data.[30,31,32] *Operando* SXRD was performed using an *in situ* electrochemical cell developed by Leriche *et al*.[33] with the electrode preparation process described in [24]. The *operando* cell was operated at the cycling rate of *C*/10 per Na^+ in the potential range of 2.5 - 4.5 V vs. Na^+/Na.

Elemental analysis. The pristine material was first completely dissolved in a mixture of concentrated hydrochloric acid and concentrated nitric acid, and inductively coupled plasma-optical emission spectroscopy was performed on the as-prepared solution in order to determine the Na: V: Fe: P relative ratio.

Mössbauer measurement. ^{57}Fe Mössbauer measurement was performed using a constant acceleration Halder-type spectrometer operating in transmission geometry with a room temperature ^{57}Co source (embedded in Rh matrix). The refinement of Mössbauer hyperfine parameters was performed using homemade programs and the WinNormos software (Wissenschaftliche Elektronik GmbH). All Mössbauer signals were analyzed using a distribution of the quadrupole splitting parameter (Δ) following the method proposed by Hesse and Rübartsch.[34]

X-ray absorption spectroscopy. Synchrotron X-ray absorption spectroscopy (XAS) spectra were recorded at the vanadium and iron K-edges' energy in transmission mode at the ROCK beamline of the SOLEIL synchrotron facility (France)[35,36] with the experimental conditions as described in [24,33]. The *ex situ* reference samples were used to determine to oxidation state of V and Fe ($V^{3+}PO_4$, $V^{5+}OPO_4$ and $LiV^{4+}PO_4O$ for V, $Fe^{2+}SO_4.7H_2O$ and $Fe^{3+}PO_4.2H_2O$ for Fe). *Operando* XAS at V K-edge was recorded on a Na//$Na_3(VO)Fe(PO_4)_2F_2$ half-cell operating in the voltage range of 2.5 - 4.5 V vs. Na^+/Na at the cycling rate of *C*/10 per Na^+. In total, 37 XAS spectra were recorded and each spectrum was an average of 690 scans recorded during 6 min and the time interval between two successive spectra is 12 min. The

energy calibration and normalization were done using graphical interfaces available on the ROCK beamline.[37] The extended X-ray absorption fine structure (EXAFS) analysis was performed using the Demeter package.[38] Fourier transforms of the k^2 weighted EXAFS oscillations were carried out in the k range from 2.6 - 13.0 $Å^{-1}$. Fitting was performed in the R range from 1.0 - 2.2 Å. EXAFS amplitudes and phase shifts were calculated by FEFF7. The coordination number of each vanadium or iron center (N = 6), the energy reference shift (E^0 = 0 eV), and the attenuation factor ($S0^2$ =1) were kept fixed during the fit. In $Na_3(VO)Fe(PO_4)_2F_2$, V resides in VO_5F while Fe resides in FeO_4F_2 octahedral site; however, in order to simplify the fitting model, we assume that six ligands surrounding vanadium or iron center are all oxygen as O^{2-} and F^- are similar X-ray scatterers. The radial distance R_i and the Debye-Waller factor σ^2 were allowed to vary during the fit. This leads to 4 parameters to refine (3 different populations of bond lengths and a common Debye Waller factor for all of them) for 7 independent parameters ($2.\Delta k.\Delta R/\pi \sim 7$).

Nuclear magnetic resonance spectroscopy. ^{31}P solid-state nuclear magnetic resonance (*ss*-NMR) spectra were recorded on a Bruker Avance III 100 MHz spectrometer, equipped with a 2.4 T widebore magnet. The powder was packed in a 2.5 mm rotor and spun at 30 kHz MAS rate. An aqueous H_3PO_4 85% (Sigma-Aldrich) solution was used as external reference. A Hahn echo sequence with a $\pi/2$ pulse length of 1.1 μs and a recycle delay of 0.2 s was used to record the ^{31}P NMR signals.

Density functional theory calculations. In paramagnetic materials, such as $Na_3V^{3+}{}_2(PO_4)_2F_3$, $Na_3(VO)_2(PO_4)_2F$, and $Na_3(VO)Fe(PO_4)_2F_2$, the NMR resonance frequency of ^{31}P nuclei in the structure depends on the strength of the electron - nuclear spin interaction (Fermi contact) between the unpaired electrons of $V^{3+}/V^{4+}/Fe^{3+}$ and the phosphorus nuclei. The Fermi contact between V^{3+}/V^{4+} and phosphorus nuclei in this structural framework has recently been reported in details [39] but nothing is known for Fe^{3+}. In order to understand the electron -

nuclear spin interaction between Fe^{3+} and phosphorus nuclei, and to assign the ^{31}P MAS NMR resonances observed in the $Na_3(VO)Fe(PO_4)_2F_2$, we performed first-principles density functional theory (DFT) calculations and evaluated the electron spin density on each phosphorus nuclei in $Na_3Fe_2(PO_4)_2F_3$ phase. Calculations using projector augmented wave (PAW) method were computed with the Vienna *ab initio* simulation package (VASP) code.[40] A wave plane cutoff energy of 600 eV and a *k*-mesh of 2x2x2 were applied. The energy minimization and the electron density on each atom in the structure were calculated using the generalized gradient approximation (GGA). Further information on the DFT calculations and their related results can be found in the supplementary information.

Electrochemical characterization. The electrochemical performance was tested in CR2032-type coin cells. The positive electrodes were prepared by mixing the active material with PTFE and carbon black (80: 10: 10 by wt.%), and then dried overnight at 80°C under vacuum. All the assembled cells were cycled in an electrolyte containing 1M of $NaPF_6$ (Strem Chemical; 99%) in ethylene carbonate and dimethyl carbonate (1: 1) with 2 wt.% of fluoroethylene carbonate at *C*/10, *C*/5, *C*/2 and *C* cycling rates in the voltage window of 2.5 - 4.3 V or 1.5 - 5.0 V vs. Na^+/Na.

3. Results and discussions

Material preparation

The XRD pattern recorded on the as-obtained $Na_3(VO)Fe(PO_4)_2F_2$ revealed that all the observed diffraction peaks could be indexed in the $P4_2/mnm$ space group. No unindexed diffraction peak was detected. Comparing the obtained powder to $Na_3V_2(PO_4)_2F_3$ and $Na_3(VO)_2(PO_4)_2F$, there is an obvious change in their color. $Na_3V_2(PO_4)_2F_3$ and $Na_3(VO)_2(PO_4)_2F$ are dark grey and bluish green due to the presence of V^{3+} and V^{4+} respectively, whereas the synthesized $Na_3(VO)Fe(PO_4)_2F_2$, with a V^{4+}/Fe^{3+} ratio equals to 1, is

beige (**Figure S1**). The ICP-OES analysis reveals a Na: V: Fe: P relative ratio of 2.9: 1: 1: 2 in this final product, which is in good agreement with the theoretical one. The SEM images of **Figure S2** show that the powder consists of well crystalline primary particles of ca. 500 nm.

Besides the synthesis of $Na_3(VO)Fe(PO_4)_2F_2$ we also explored the extended composition domain $Na_3(VO)_{2-y}Fe_y(PO_4)_2F_{1+y}$ ($0 \leq y \leq 2$) by varying the $V(C_5H_7O_3)_3$: $Fe(NO_3)_3.9H_2O$ molar ratio in the initial solution. The syntheses were performed in the same conditions as those already discussed, however the obtained powders were a mixture of NVPF- and NASICON-type phases (**Figure S3**). We also varied the thermal treatment conditions, but no pure phase was successfully obtained (**Figure S4**).

Atomic and electronic structural description

The $Na_3V_2(PO_4)_2F_3$ parent composition presents a subtle orthorhombic distortion of the unit cell as detected by SXRD through the splitting of the (200)/(020) and (400)/(040) diffraction peaks and is now indexed in the *Amam* space group.[8] In the newly obtained Fe-substituted $Na_3(VO)Fe(PO_4)_2F_2$ phase, no obvious separation of the (200)/(020) and (400)/(040) doublets are observed suggesting that the structure should be indexed in the $P4_2/mnm$ space group. Rietveld refinements were performed in the *Amam* (**Figure S5**) and in the $P4_2/mnm$ space groups (**Figure 2**) in order to choose the best structural description for this newly obtained phase. As especially highlighted by a comparison of the profile fittings, the reliability factors, the cell parameters and the interatomic distances (given in **Figure 2**, **Figure S5** and **Table S1)**, no improvement of the fit was observed by considering the orthorhombic symmetry, and hence the tetragonal unit cell was thus retained. Three Na^+ positions were identified in the structure using Fourier difference maps, the details of this procedure are described in **Figure S6** and **S7**. The atomic positions and the obtained bond length values are given in **Table 1** and **Table 2**, respectively. The M–F(2)/O(4) distance, which corresponds to the terminal bonds of the bi-octahedron, is rather short (1.795(1) Å) and is equal to the average

value between the V=O bond length in $Na_3(VO)_2(PO_4)_2F$ and the terminal Fe–F bond length in $Na_3Fe_2(PO_4)_2F_3$ (1.626(1) Å and 1.92(1) Å, respectively).[24,41,42] This observation strongly suggests the presence of V=O bonds in the structure of this newly obtained $Na_3(VO)Fe(PO_4)_2F_2$ phase.

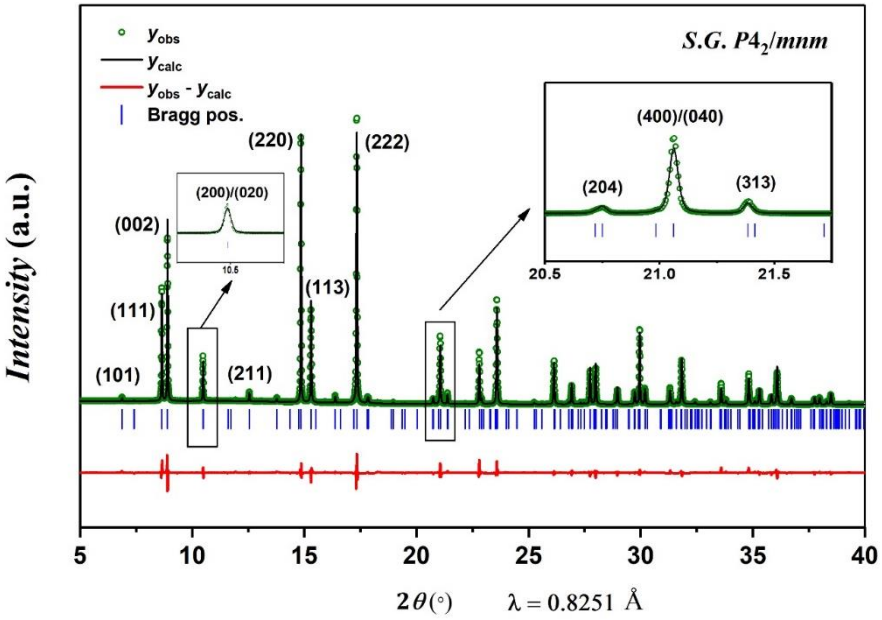

Figure 2 : Rietveld refinement of the $Na_3(VO)Fe(PO_4)_2F_2$ structure from SXRD data, performed in the $P4_2/mnm$ space group. Insets show enlargements of the (200)/(020) and (400)/(040) doublets.

Table 1 : Structural parameters of $Na_3(VO)Fe(PO_4)_2F_2$ obtained from Rietveld refinement of synchrotron powder diffraction data collected at λ = 0.8251 Å. The Biso values of oxygen and fluorine were fixed during the Rietveld refinement.

S.G. $P4_2/mnm$	$a = b = 9.03564(6)$ Å		$R_{Bragg} = 3.46\%$
$Z = 4$	$c = 10.6412(1)$ Å		$R_p = 10.3\%$
	$V/Z = 217.195(2)$ Å^3		$R_{wp} = 10.7\%$

Atoms	**Wyckoff positions**	***x/a***	***y/b***	***z/c***	**Occupancy**	**B_{iso}**
V(1)	8j	0.7483(6)	0.2517(6)	0.1917(2)	½	0.96(6)
Fe(1)	8j	0.7483(6)	0.2517(6)	0.1917(2)	½	0.96(6)
P(1)	4e	½	½	0.253(2)	1	0.9(1)
P(2)	4d	½	0	¼	1	0.8(1)

O(1)	16k	0.595(2)	0.094(2)	0.162(1)	1	0.78
O(2)	8j	0.598(2)	0.402(2)	0.160(2)	1	0.78
O(3)	8j	0.402(2)	0.402(2)	0.330(2)	1	0.78
O(4)	8j	¾	¼	0.360(2)	½	1.0
F(1)	4g	¾	¼	0	1	0.44
F(2)	8j	¾	¼	0.360(2)	½	1.0
Na(1)	8i	0.270(2)	0.022(2)	0	0.850(3)	2.1(1)
Na(2)	8i	0.476(3)	0.290(3)	0	0.58(1)	4.5(4)
Na(3)	4f	0.408(5)	0.408(5)	0	0.266(6)	3.0(3)

Table 2 : Bond lengths (Å) describing the coordination polyhedra of each cation in $Na_3(VO)Fe(PO_4)_2F_2$ determined from Rietveld refinement performed in the $P4_2/mnm$ space group of synchrotron X-ray powder diffraction data collected at $\lambda = 0.8251$ Å.

	V/Fe	P(1)	P(2)	Na(1)	Na(2)	Na(3)
Coordination	6	4	4	7	7	6
O(1)	1.954(6)	1.595(8)x2		2.619(9)x2	2.27(1)x2	2.42(1)x4
O(2)	2.013(6)		1.529(6) x4		2.70(1)x2	
O(3)	1.983(6)x2	1.493(8)x2		2.351(7)x2		
F(1)	2.040(1)			2.464(7)	2.50(1)	
F(2)/O(4)	1.795(1)			2.547(6)x2	2.55(1)x2	2.50(1)x2

The ^{57}Fe Mössbauer spectrum of this sample exhibits a single quadrupole doublet (**Figure 3a**) with an isomer shift $\delta = 0.41(1)$ mm·s^{-1} and a mean quadrupole splitting $\Delta = 0.61$ mm·s^{-1} corresponding to six-fold coordinated high spin Fe^{3+} ion (t_{2g}^3 e_g^2) in a highly symmetric environment. The rather high value of isomer shift is due to the high ionic character of the Fe–F and Fe–O bonds. The quadrupole splitting distribution is mono-modal and very narrow meaning that there is only one discrete site (*8j*) for Fe^{3+} ions with a regular and non-disordered local environment (**Figure S8** and **Table S2**).[43]

X-ray absorption near edge structure (XANES) at vanadium K-edge (5465 eV) and at iron K-edge (7112 eV) spectra were recorded in order to determine the local environment as well as the oxidation state of vanadium and iron species in the structure. Each XANES spectrum can be divided into the pre-edge and the edge regions. For 3*d* transition metals, the pre-edge signal is related to the forbidden $1s \rightarrow 3d$ transition and its intensity can be used to evaluate the local symmetry of the metal center of interest while the intense edge signal is caused by the allowed $1s \rightarrow 4p$ transition and its position is related to the metal oxidation state and the bond length values with its surrounding ligands. If the metal center resides in a highly symmetric octahedral site with the point group O_h, the $1s \rightarrow 3d$ transition is completely forbidden and the pre-edge signal is very weak or completely diminished. If the metal center resides in a distorted octahedral or tetrahedral site, the O_h symmetry is broken and the 3*d* orbitals can now be hybridized with the 4*p* orbitals. Thanks to the 3*d* - 4*p* orbital hybridization, the electron transition in the pre-edge region is allowed, which leads to a great increase in the pre-edge signal.[44] The pre-edge and the edge energies of the XANES spectra recorded at vanadium and iron K-edges confirm the expected occurrence of V^{4+} and Fe^{3+} in the pristine sample (**Figure 3b-c**). The low intensity of the pre-edge signal on the XANES spectrum at Fe K-edge confirms the symmetrical octahedral environments of high-spin Fe^{3+}, while the high intensity of the pre-edge on the V K-edge spectrum implies that V local environment is highly distorted due to the presence of the highly covalent vanadyl bond, which is in agreement with the bond length values obtained from Rietveld refinement.

While the V^{4+} and Fe^{3+} ions share the same Wyckoff position in the structure and hence cannot be distinguished by SXRD, the EXAFS analysis at both V and Fe K-edges provides detailed information about the $V(O,F)_6$ and $Fe(O,F)_6$ local environments, even if oxygen and fluorine cannot be distinguished. The EXAFS analysis at Fe K-edge of the $Na_3(VO)Fe(PO_4)_2F_2$ spectrum shows that the Fe^{3+} occupies an octahedral environment and is coordinated by four O

atoms in a square plane at a distance of 2.00 Å and two O/F atoms on the axial positions at distances of 1.90 Å and 2.00 Å, with Debye-Waller factors of $4.99 \cdot 10^{-3}$ Å^2. On the other hand, the $V^{4+}(O,F)_6$ octahedron is built by four equivalent O atoms in a square plane at a V–O distance of ~ 2.00 Å, one O/F atom at 2.11 Å, and a closer O/F at 1.65 Å corresponding to the V=O vanadyl-type bond. Smaller Debye-Waller factors ($2.24 \cdot 10^{-3}$ Å^2 vs $4.99 \cdot 10^{-3}$ Å^2) are observed, which is in good agreement with a more covalent environment for V^{4+} than for Fe^{3+}. Taking into account the stoichiometry as well as the vanadium and iron oxidation states, the structure of $Na_3(VO)Fe(PO_4)_2F_2$ can be described as FeO_4F_2 and VO_5F octahedra which are sharing one common fluorine atom to form $FO_4Fe–F–FeO_4F$, $FO_4Fe–F–VO_5$, or $O_5V–F–VO_5$ bi-octahedral units. Indeed, no superstructure corresponding to the V^{4+}/Fe^{3+} ordering was detected in the SXRD data. The two ions are randomly distributed over all the transition metal sites in the structure.

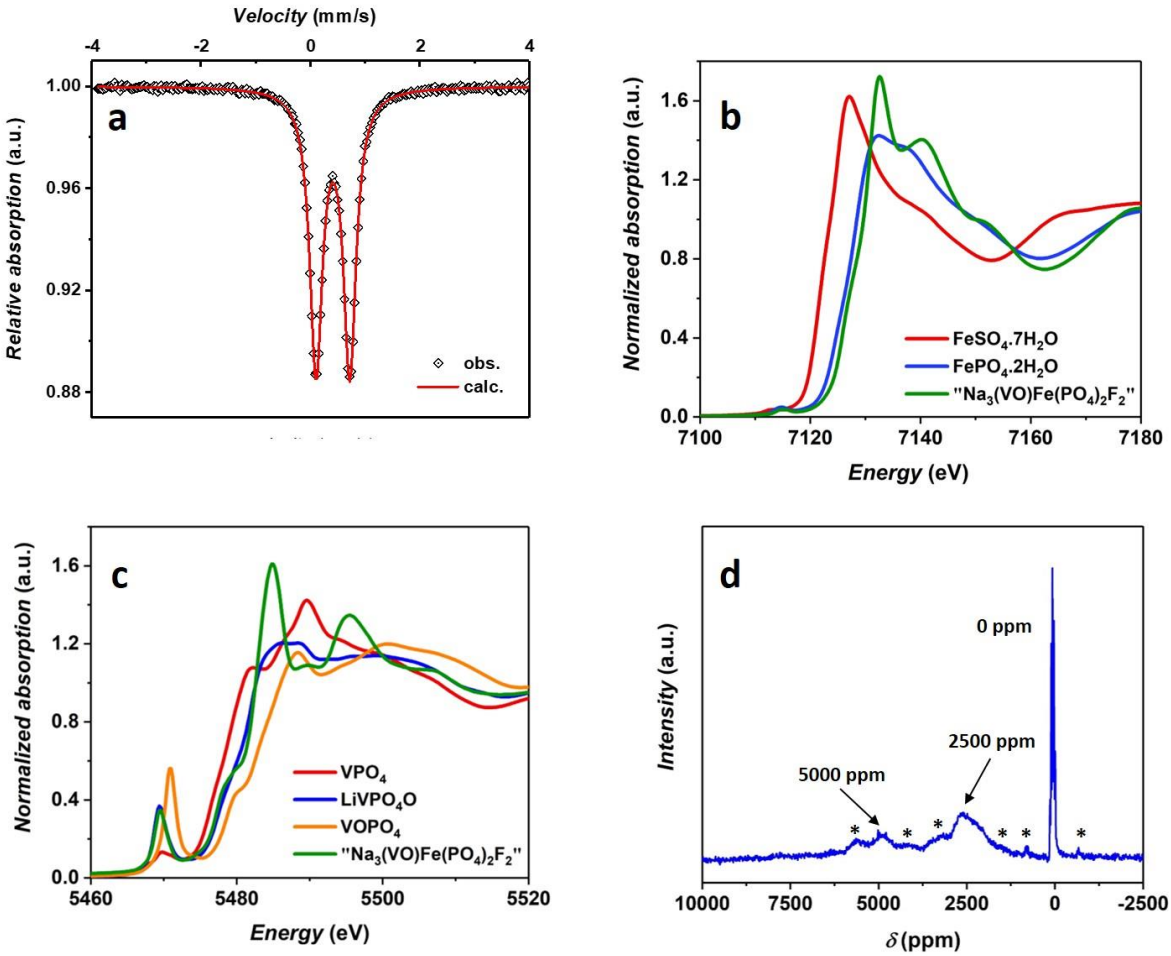

Figure 3 : (*a*) ^{57}Fe Mössbauer spectrum recorded at ambient temperature with a ^{57}Co source, (*b*) Fe K-edge XANES spectrum of $Na_3(VO)Fe(PO_4)_2F_2$. Both $Fe^{2+}SO_4.7H_2O$ and $Fe^{3+}PO_4.2H_2O$ are used as references to determine the Fe oxidation state, (*c*) V K-edge XANES spectrum of $Na_3(VO)Fe(PO_4)_2F_2$. The $V^{3+}PO_4$, $LiV^{4+}PO_4O$ and $V^{5+}OPO_4$ XANES spectra are reported to determine the V oxidation state, (*d*) ^{31}P *ss*-NMR spectrum recorded at 100 MHz, MAS frequency = 30 kHz. The excitation pulse was placed at 5000 ppm. The asterisks (*) indicate the rotational spinning sidebands.

The ^{31}P ss-NMR spectrum of the sample shows the possible presence of several resonances in the range of 0 to 10000 ppm (**Figure 3d**). We have recently demonstrated that the presence of V^{4+} ion in highly distorted octahedral sites in this structure will cause no Fermi contact with the neighboring phosphorus nuclei as the orbital containing the electron spin of V^{4+} does not point towards the phosphorus sites and the ^{31}P resonance at ~ 0 ppm is associated to the $P(OV^{4+})_4$ local environment.[39] Therefore, ^{31}P paramagnetic resonances observed here can only be induced by the Fermi contact between Fe^{3+} and phosphorus nuclei. This Fermi contact

is studied through the $Na_3Fe_2(PO_4)_2F_3$ crystal structure and is described in details in **Figure S9** and **Table S3**. The obtained results show that the Fe^{3+} ions in $Na_3(VO)Fe(PO_4)_2F_2$ are in the high-spin state (t_{2g}^3 e_g^2) with five unpaired electrons; these electron spins can be transferred from Fe^{3+} to the neighboring phosphorus nuclei through the $d_{xz}/d_{yz}(Fe^{3+})-2p(O)-sp^3(P)$ orbital hybridization. All the phosphorus nuclei in $Na_3Fe_2(PO_4)_2F_3$ are surrounded by four Fe^{3+}, forming the unique $P(OFe^{3+})_4$ local environment with a paramagnetic shift of ~ 8400 ppm (**Figure S9**). As we have recently shown that the paramagnetic interaction in this structural framework is cumulative,[39] which implies that the presence of one Fe^{3+} in the proximity of a phosphorus nuclei will contribute to a paramagnetic shift value of ~ 2100 ppm. We thus deduce that the $P(OV^{4+})_3(OFe^{3+})$, $P(OV^{4+})_2(OFe^{3+})_2$, and $P(OV^{4+})(OFe^{3+})_3$ local environments, if they exist in this crystal structure, should give rise to the ^{31}P NMR resonances at ~ 2100 ppm, 4200 ppm, and 6300 ppm, respectively. The experimental signals are indeed observed in this range, but unfortunately the signals are really broad due to a strong dipolar interaction between the five unpaired electrons of each Fe^{3+} and the phosphorus nucleus. These broad signals also overlap with the spinning side bands and the resolution of the recorded spectrum is not sufficient to detect all individual contributions.

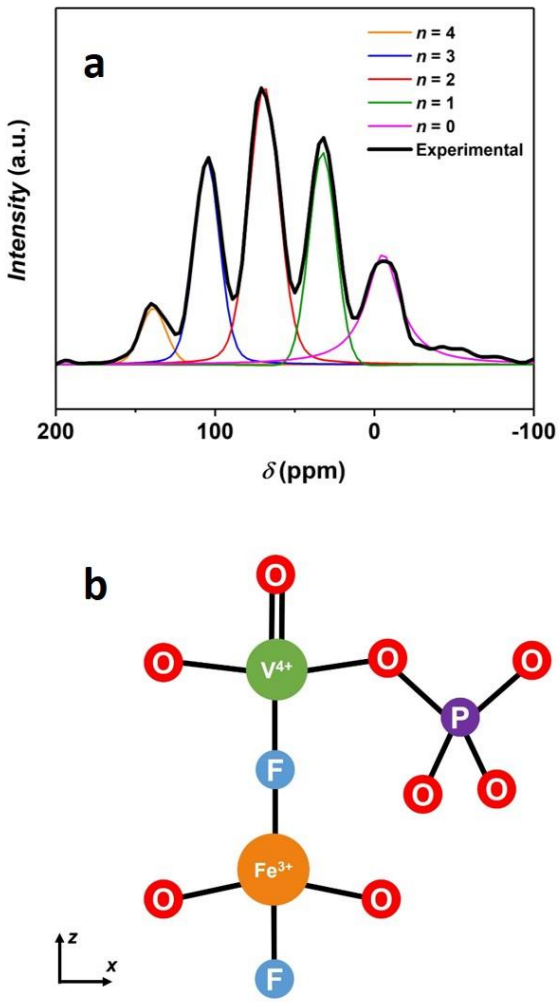

Figure 4 *:* (*a*) An enlargement of the ^{31}P NMR diamagnetic resonances (-100 ppm to 200 ppm) recorded for the $Na_3(VO)Fe(PO_4)_2F_2$ material. The *n* value indicates the number of Fe^{3+} in the second transition metal sites with respect to the Phosphorus nucleus. The five diamagnetic resonances observed for this material can be fitted by five different Pseudo-Voigt peak shape functions, (*b*) Illustration of the influence of the second neighboring metal ion belonging to the bi-octahedral unit on the ^{31}P chemical shift value.

An enlargement on the ^{31}P NMR diamagnetic region associated to the $P(OV^{4+})_4$ environment (from -100 ppm to 200 ppm) reveals the presence of five diamagnetic resonances equally separated by ~ 35 ppm. They can be fitted by five different Pseudo-Voigt peak shape functions (**Figure 4a**) and the corresponding values for the chemical shift, peak width and amplitude are compared in **Table S4**. As a V^{4+} ion in this structure induces almost no Fermi contact with the neighboring P,[39] these small shifts are associated to the presence of Fe^{3+} ions

in the second coordination sphere of ^{31}P nucleus leading either to a weak Fermi contact shift or to small changes in the local atomic or electronic structure around V^{4+} resulting in such a small shift. These five ^{31}P NMR resonances correspond to $P(OV^{4+})_4$ local environments with different distribution of V^{4+} : Fe^{3+} as second neighbors in the bi-octahedral units (**Figure 4b**). We hence propose that each Fe^{3+}, as second transition metal neighbor in the bi-octahedra, contributes to a shift of ~35 ppm; therefore, the resonances at ~0 ppm, 33 ppm, 69 ppm, 105 ppm, and 139 ppm are assigned to $P(OV^{4+}\text{─}F\text{─}V^{4+})_{4-n}(OV^{4+}\text{─}F\text{─}Fe^{3+})_n$ local environments with n = 0, 1, 2, 3, 4, respectively. The relative intensities of the five diamagnetic resonances are in agreement with the values estimated considering a binomial distribution (**Table S4**). This shows that the V^{4+}/Fe^{3+} distribution in the bi-octahedral units is fully random and solely controlled by statistics.

All the information obtained by SXRD, chemical analyses, as well as the local structure description determined by ^{57}Fe Mössbauer, ^{31}P NMR and XAS at V and Fe K-edges spectroscopies, fully support the chemical formula $Na_3(V^{4+}O)Fe^{3+}(PO_4)_2F_2$ proposed from the very beginning of the paper.

Electrochemical properties of $Na_3(VO)Fe(PO_4)_2F_2$

$Na_3(VO)Fe(PO_4)_2F_2$ was investigated as positive electrode in SIBs and cycled in the voltage window 2.5 - 4.3 V vs. Na^+/Na at the cycling rate of *C*/10 per Na^+; only one Na^+ can be reversibly extracted in this voltage window (**Figure 5a**). The first derivative curve for $Na_3(VO)Fe(PO_4)_2F_2$ shows the presence of a broad peak at ~ 3.64 V vs. Na^+/Na (Inset of **Figure 5a**), which is similar to that observed for the V^{5+}/V^{4+} redox couple involved during Na^+ extraction and re-insertion from/in the $Na_3(VO)_2(PO_4)_2F$ counterpart.[9]

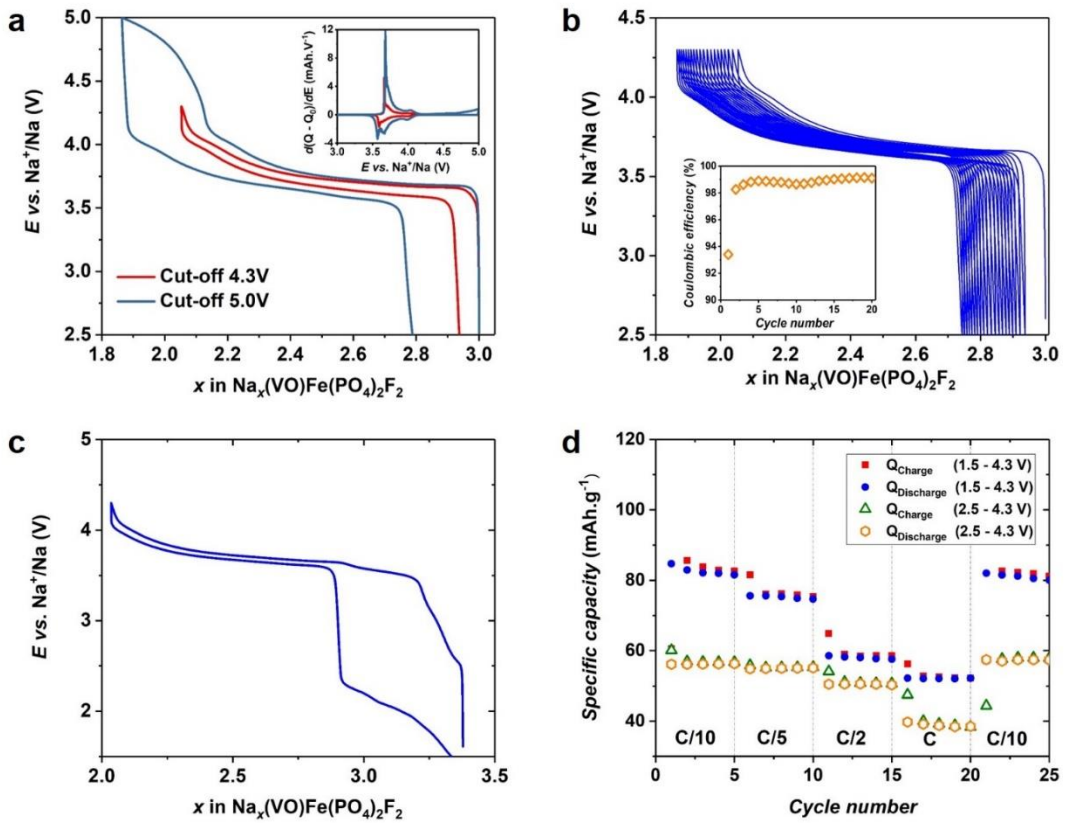

Figure 5 : (*a*) The charge/discharge curve of $Na_3(VO)Fe(PO_4)_2F_2$ vs. Na metal, at *C*/10 cycling rate with the cut-off voltage of 4.3 and 5.0 V. Inset shows the first derivative charge/discharge curve as a function of the operating voltage, (*b*) The long-term evolution of the charge/discharge curves at *C*/10 cycling rate in the potential range of 2.5 - 4.3 V vs. Na^+/Na. Inset shows the evolution of the coulombic efficiency during the first twenty cycles, (*c*) The charge/discharge curve obtained at the second cycle for $Na_3(VO)Fe(PO_4)_2F_2$ vs. Na metal, at *C*/10 per Na^+ and in the potential range of 1.5 - 4.3 V vs. Na^+/Na, (*d*) The charge/discharge capacity of $Na_3(VO)Fe(PO_4)_2F_2$ at different cycle rates in the potential ranges of 2.5 - 4.3 V and 1.5 - 4.3 V vs. Na^+/Na.

Several intermediate phases, stabilized by the Na^+–vacancy ordering, were detected during the Na^+ extraction and re-insertion from/in $Na_3(VO)_2(PO_4)_2F$ [9]; in the case of $Na_3(VO)Fe(PO_4)_2F_2$, the electrochemical profile shows that the voltage increases/decreases continuously during charge/discharge and thus suggests a solid solution mechanism. Indeed, Fe^{3+} is randomly distributed among the transition metal sites, which thus prevents the formation of charge ordering on the transition metal sites as well as the Na^+–vacancy ordering within the diffusion channels of the host structure. Extra capacity is observed when the upper cut-off voltage is increased up to 5.0 V; nevertheless, this capacity is irreversible (**Figure 5a**). As this

material contains only one V^{4+} ion per formula unit, the extraction of one Na^+ implies that all the vanadium ions are at the pentavalent state in $Na_2(VO)Fe(PO_4)_2F_2$. Then, the extra capacity can either be attributed to the oxidation of Fe^{3+} into Fe^{4+} or to the electrolyte degradation. Nonetheless, the ^{57}Fe Mössbauer spectrum recorded on the sample recovered at 5.0 V only shows the presence of Fe^{3+} in its high-spin state (**Figure S8**) confirming that Fe^{3+} was not oxidized into Fe^{4+}. We thus conclude that this irreversible extra capacity is attributed to the electrolyte decomposition.

Even without carbon-coating, this material shows very small polarization with limited capacity fading during cycling (**Figure 5b Inset**). Indeed, comparing to a $Na//Na_3(VO)_2(PO_4)_2F$ half-cell operating in the same conditions, the polarization observed for a $Na//Na_3(VO)Fe(PO_4)_2F_2$ half-cell appears to be two times smaller (**Figure S10**). The cell parameters and the size of the diffusion channels of $Na_3(VO)Fe(PO_4)_2F_2$ are only ~ 0.1% bigger than those of $Na_3(VO)_2(PO_4)_2F$; furthermore, the primary particles of $Na_3(VO)Fe(PO_4)_2F_2$ are even bigger than those of $Na_3(VO)_2(PO_4)_2F$ indicating that the easier diffusion cannot be attributed to shorter diffusion lengths (**Figure S11**). These results suggest that the smaller polarization observed for $Na_3(VO)Fe(PO_4)_2F_2$ is due to an improvement in the intrinsic properties of the material. Dacek *et al*. reported that Na^+ diffusivity in $Na_3M_2(PO_4)_2X_3$ (M = Al, V, Ti; X = F, O) and in similar structures is unlikely affected by the size of the diffusion channels. It would rather depend strongly on the Na^+–vacancy ordering and the Na^+-defect formation energy.[45,46] A material with a high tendency to form Na^+–vacancy ordering upon cycling, such as $Na_3V_2(PO_4)_2F_3$ and $Na_3(VO)_2(PO_4)_2F$, will have a slower Na^+ diffusion process as extra activation energy is required to first break the Na^+–vacancy ordering and then create local defects for the diffusion to occur.[45] Any factor, such as cationic substitution on the vanadium site,[45,46] that can prevent the formation of Na^+–vacancy ordering during charge or lower the Na^+-defect formation energy will thus be a driving force for the formation of off-

stoichiometry compositions. Therefore, Fe^{3+} substitution for V with a random distribution of Fe^{3+} over V sites can be considered as an appropriate substituent or dopant that can be used to improve the Na^+ diffusivity in $Na_3V_2(PO_4)_2F_3$ and $Na_3(VO)_2(PO_4)_2F$-type materials.

Extra reversible capacity is obtained when the lower cut-off voltage is decreased to 1.5 V vs. Na^+/Na (**Figure 5c**), which could be due to the activation of the Fe^{3+}/Fe^{2+} redox couple that had been reported earlier for the $Na_3Fe_2(PO_4)_2F_3$ composition.[47] The ^{57}Fe Mössbauer spectrum recorded on the material recovered at 1.5 V reveals the existence of 47% of Fe^{2+} (isomer shift $\delta = 1.26$ mm·s^{-1}) and 53% of Fe^{3+} ($\delta = 0.42$ mm·s^{-1}) in their high-spin state confirming the occurrence of the Fe^{3+}/Fe^{2+} redox couple in this voltage region (**Figure S8**). Other hyperfine parameters of these iron species are given in **Table S2**. The hyperfine parameters of Fe^{3+} in the pristine phase and in $Na_{3.5}(VO)Fe(PO_4)_2F_2$ are very similar implying that there is little influence of the second coordination sphere on the Fe^{3+} sites. The reduction of 0.47 Fe^{3+} to Fe^{2+} corresponds to the insertion of extra ~ 0.5 Na^+ ion at the low voltage region and leads to the composition $Na_{3.5}(VO)Fe(PO_4)_2F_2$. The insertion of more than 0.5 Na^+ ion into the structure is not achieved, even at low cycling rates, most probably due to the strong Na^+–Na^+ electrostatic repulsions within the channels of the structure that destabilizes the formation of the phases with more than 3.5 Na^+ per formula unit. Zhang *et al*. reported that $Na_4V_2(PO_4)_2F_3$ could be synthesized mechanically by ball milling $Na_3V_2(PO_4)_2F_3$ with Na metal.[48] Three Na^+ ions were electrochemically extracted from $Na_4V_2(PO_4)_2F_3$ upon charge; however, only two Na^+ ions could be reinserted into the structure during discharge to form $Na_3V_2(PO_4)_2F_3$. The initial phase, $Na_4V_2(PO_4)_2F_3$, was never recovered even though a very low cut-off voltage was applied.[48] These observations confirm our results that the NVPF-like structure cannot accommodate so many Na^+ into its structural channels. The polarization increases greatly when the lower cut-off voltage is set at 1.5 V (**Figure 5c**), suggesting that the Fe^{3+}/Fe^{2+} reduction and the extra Na^+ insertion processes are not energetically favorable; nevertheless, it appears that

the presence of a huge polarization at low voltage does not affect the electrochemical mechanism involving the V^{5+}/V^{4+} redox couple at the high voltage region. By opening the electrochemical window to 1.5 - 4.3 V, the Fe^{3+}/Fe^{2+} redox couple can thus be activated, which leads to an increase of the reversible capacity of ca. 50% at *C*/10 (**Figure 5d**). Furthermore, it can recover its initial capacity delivered at *C*/10 after a series of cycling at higher rates (**Figure 5d**).

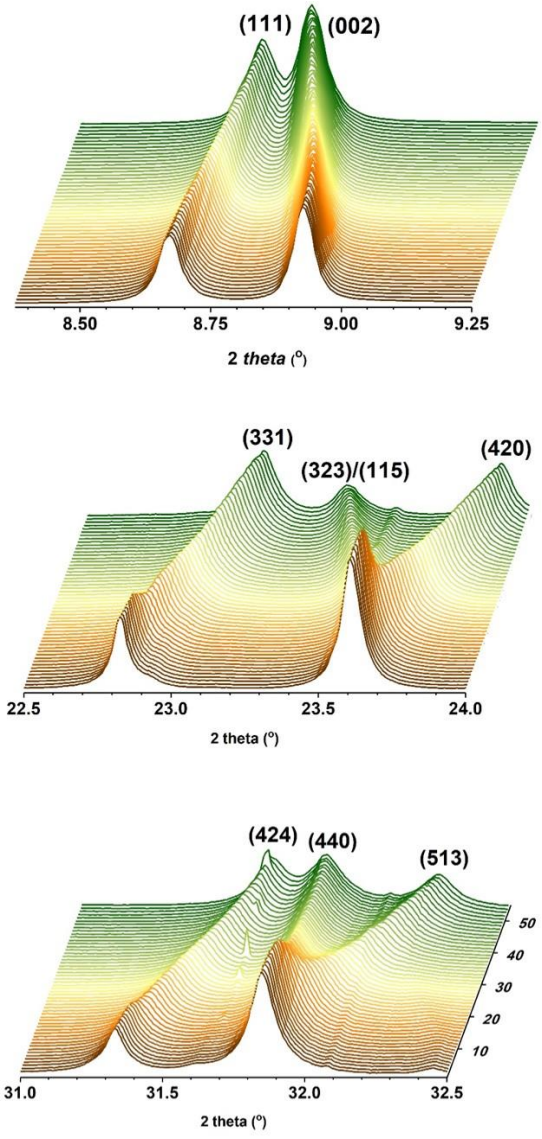

Figure 6 : The evolution of significant diffraction lines during Na^+ de-intercalation from $Na_3(VO)Fe(PO_4)_2F_2$. *Operando* SXRD patterns were recorded upon cycling of a Na// $Na_3(VO)Fe(PO_4)_2F_2$ half-cell at λ = 0.8251 Å. The cell was cycled at C/10 cycling rate in the voltage window of 2.5 - 4.3 V vs. Na^+/Na. The corresponding electrochemical data is given in **Figure S12**.

Operando X-ray diffraction patterns recorded upon charging of an electrochemical Na//$Na_3(VO)Fe(PO_4)_2F_2$ half-cell in the potential range of 2.5 - 4.3 V show a continuous evolution of the diffraction lines during the operation (**Figure 6**). This confirms the solid solution mechanism involved in the Na^+ de-intercalation process, as suggested by the continuous evolution of the voltage profile (**Figure S12**). As expected for a solid solution mechanism, the description of the structure in the tetragonal unit cell ($P4_2/mnm$ S.G.) remains valid all along the Na^+ de-intercalation. The Le Bail fit of $Na_{2.54}(VO)Fe(PO_4)_2F_2$ in the $P4_2/mnm$ space group, recorded at pattern #25, is given in **Figure S13**. The cell parameters of $Na_{3-x}(VO)Fe(PO_4)_2F_2$ evolve slowly during the first five patterns, which could be due to a delay in the reaction at the beginning of charge; nevertheless, a linear evolution is observed from the sixth pattern until the end of charge (**Figure 7**).

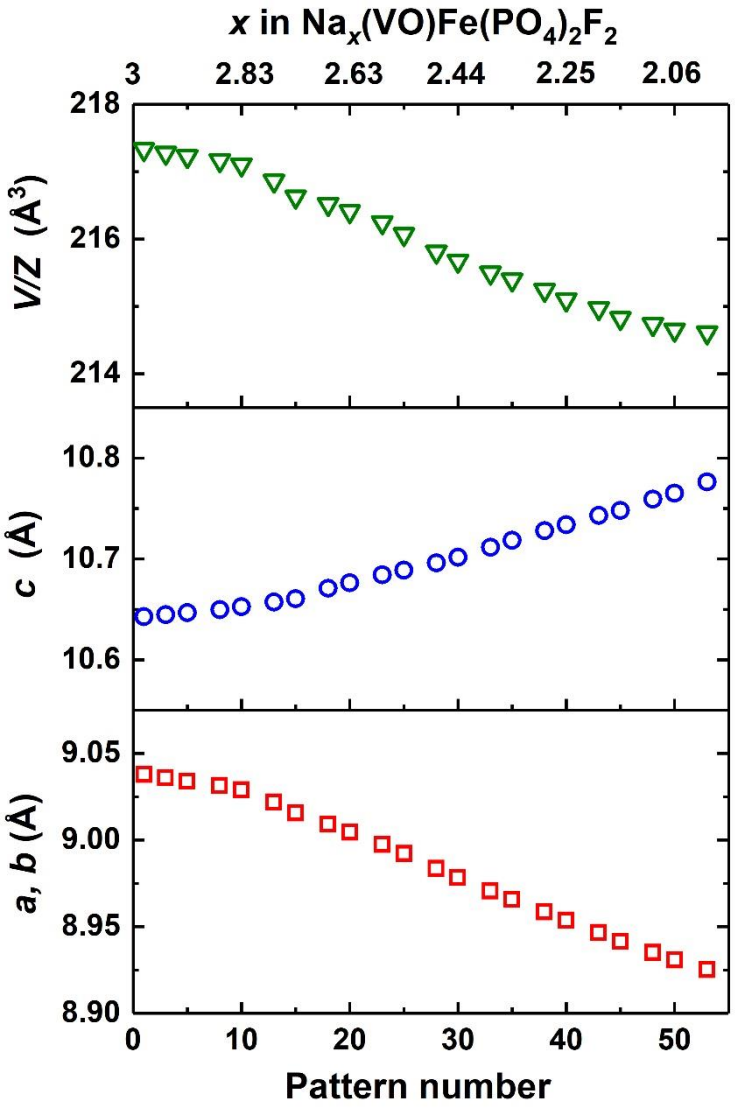

Figure 7 : The evolution of the cell parameters of $Na_{3-x}(VO)Fe(PO_4)_2F_2$ during the Na^+ de-intercalation reaction, determined from the Le Bail fit of the SXRD patterns collected *operando* upon charging a $Na//Na_3(VO)Fe(PO_4)_2F_2$ half-cell.

The cell volume decreases with a contraction of the structure along *a* and *b* directions and an expansion along the *c* direction during charge (**Figure 7**). As expected, the oxidation of V^{4+} into V^{5+} with a smaller ionic radius leads to the decrease of *a* and *b*, whereas the Na^+ de-intercalation decreases the screening effect between the terminal groups of two bi-octahedral units pointing directly towards each other "through" the channel (**Figure 1**) and thus results in an increase of the *c* parameter as a compensation effect. This anisotropic contraction/expansion

of the unit cell during the Na^+ de-intercalation reaction was also observed in $Na_3V_2(PO_4)_2F_3$, $Na_3(VO)_2(PO_4)_2F$ as well as many NASICON materials.[9,12,13,49]

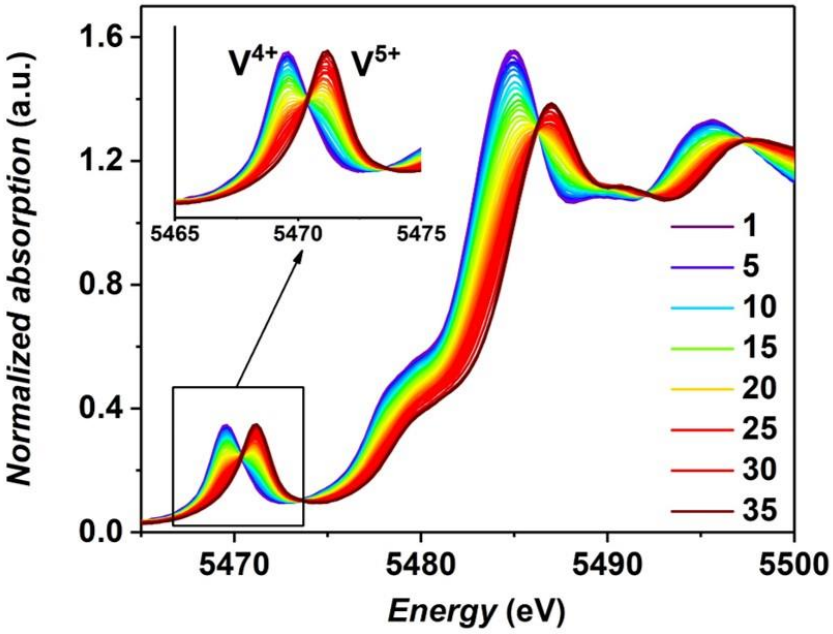

Figure 8 : Vanadium K-edge XANES spectra recorded *operando* upon charging a $Na//Na_3(VO)Fe(PO_4)_2F_2$ half-cell operating in the potential range of 2.5 - 4.5 V vs. Na^+/Na (**Figure S14**).

Operando XAS spectra at vanadium K-edge were collected upon charging a $Na//Na_3(VO)Fe(PO_4)_2F_2$ half-cell in the voltage range of 2.5 - 4.5 V at *C*/10 (**Figure 8**); note that *operando* XAS experiment at Fe K-edge were not performed as ^{57}Fe Mössbauer measurements performed *ex situ* had already demonstrated that Fe^{3+} did not participate in the electrochemical reaction in the high voltage region. A linear evolution of the vanadium absorption edge is observed between 2.5 and 4.3 V (**Figure S15**). Above 4.3 V, no change in the shape or the absorption edge energy is observed. The edge energy in the initial state (5481.8 *e*V, taken at 80% of the maximum intensity of the edge) corresponds to the presence of V^{4+} while at the end of the charge only V^{5+} is detected (5484.1 *e*V) (**Figure S16**), supporting the speculation on participation of the V^{5+}/V^{4+} redox couple in this potential range. The *operando*

V K-edge XAS dataset was globally analyzed using the chemometric approach, based on a combination of Principal Component Analysis (PCA) and Multivariate-Curve Resolution Alternating Least Squares (MCR-ALS).[50]

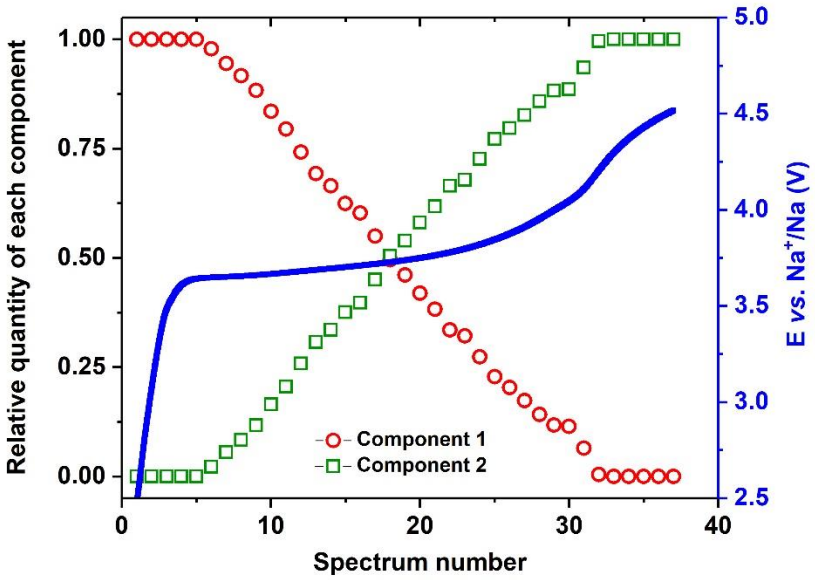

Figure 9 : The evolution of the concentration of the two principal components required to describe all the recorded Vanadium K-edge XAS spectra.

PCA allows to determine the minimum number of independent components required to describe the whole *operando* dataset obtained during the electrochemical cycling. The number of principal components is then used as the basis for the MCR-ALS analysis [51,52], allowing the reconstruction of the principal orthogonal components needed to interpret the whole dataset. The details about the chemometric analysis are reported in the supplementary information (**Figure S17**). The PCA results show that there are two components required to describe the whole system and the concentration profile of these two components is given in **Figure 9**. There is a delay in the electrochemical reaction as the vanadium oxidation state only started to change from the spectrum #5, and the electrochemical reaction involving the V^{5+}/V^{4+} redox couple finished at spectrum #33, which corresponds to a voltage value of ~ 4.3 V vs. Na^+/Na. The

reconstructed XAS spectra of these two components are identical to the spectrum #1 and spectrum #33 recorded experimentally.

The V local environments of the two principal components were obtained by analyzing the EXAFS oscillations of the reconstructed spectra. The local structure of the first component is identical to those of the pristine $Na_3(VO)Fe(PO_4)_2F_2$ reported above, which is a highly distorted $V(O/F)_6$ octahedral site due to the presence of a vanadyl bond. At the end of charge, V^{4+} is fully oxidized into V^{5+} and its local environment is even more distorted with a contraction of the bond lengths in the equatorial plane: two of the four equatorial V–O bonds are rather short (1.86 Å) while the other two are at located at a distance of 1.98 Å. The vanadyl bond ($d_{V=O}$ = 1.62 Å) and the V–F bond ($d_{V\text{-}F\ (axial)}$ = 2.10 Å) along the *c* axis are unlikely to be affected by the oxidation of V^{4+} to V^{5+}. The EXAFS analysis cannot distinguish whether the two contracted equatorial V–O bonds are in the *cis*- or in the *trans*-configuration; however, we here propose that the two short V–O bonds would rather be formed on the *trans*-positions, which allows to minimize the electrostatic repulsion between the two oxygen atoms that are approaching the V^{5+} center as a result of the bond length contraction.

4. Conclusions

$Na_3(VO)Fe(PO_4)_2F_2$ was obtained by a sol-gel method and the structure of this newly obtained phase was described in the $P4_2/mnm$ space group. Only one Na^+ can be reversibly extracted in the potential range of 2.5 - 4.3 V vs. Na^+/Na, which corresponds to the oxidation of all V^{4+} ions into V^{5+}. Limited polarization value and good capacity retention was observed upon cycling, even if the reversible capacity decreased as the Fe^{4+}/Fe^{3+} redox couple could not be activated. On the contrary, extra 0.5 Na^+ could be reversibly inserted into the structure by activating the Fe^{3+}/Fe^{2+} redox couple, but at very low voltage (~ 1.5 V vs. Na^+/Na). *Operando*

synchrotron X-ray powder diffraction revealed there was no formation of Na^+–vacancy ordering during charge (*i.e.* Na^+ de-intercalation), which was contrary to what had been observed for $Na_3V_2(PO_4)_2F_3$ and $Na_3(VO)_2(PO_4)_2F$. Their suppression would lower the Na^+-defect formation energy, and hence increase the Na^+ ionic conductivity in the diffusion channels, and could explain the low polarization value observed for this material when used at the positive electrode in a sodium cell. We hence suggest that Fe^{3+} is a promising substituent or dopant that needs to be extensively studied in order to enhance the electrochemical performance of $Na_3V_2(PO_4)_2F_3$, $Na_3(VO)_2(PO_4)_2F$ and similar phases.

Corresponding Author:

*E-mail: Laurence.Croguennec@icmcb.cnrs.fr

Notes

The authors declare no competing financial interest.

Acknowledgements:

The authors thank the RS2E Network for the funding of LHBN's PhD thesis. The European Union's Horizon 2020 research and innovation program under the Grant Agreement No. 646433-NAIADES, the French National Research Agency (STORE-EX Labex Project ANR-10-LABX-76-01 and SODIUM Descartes project ANR-13-DESC-0001-02) and the Région Nouvelle Aquitaine are acknowledged for their financial support. The authors also want to thank Cathy DENAGE, Emmanuel PETIT, Eric LEBRAUD, Alain WATTIAUX and Yohan BIECHER (ICMCB) for their technical support. The Synchrotron diffraction experiments were performed at the MSPD beamline at ALBA Synchrotron with the collaboration of ALBA staff and CALIPSOplus (Grant 730872) funding. XAS experiments were performed on the ROCK beamline at SOLEIL synchrotron, which is benefiting from a public grant overseen by the French National Research Agency as part of the "*Investissements d'Avenir*" program (Reference: ANR-10-EQPX-45).

Supporting Information

The Supporting Information is available free of charge on the ACS Publications website at DOI:

- Comparing the color of $Na_3V_2(PO_4)_2F_3$, $Na_3(VO)Fe(PO_4)_2F_2$, and $Na_3(VO)_2(PO_4)_2F$ powder (Figure S1); SEM images of $Na_3(VO)Fe(PO_4)_2F_2$ at different magnifications (Figure S2); XRD patterns of the powder obtained at different V : Fe ratios (Figure S3); Color of the powder obtained for different V: Fe ratios after a calcination at 550°C under Ar atmosphere during 3h (Figure S4); Result of the Rietveld refinement performed in the *Amam* space group on the synchrotron XRD data recorded on the $Na_3(VO)Fe(PO_4)_2F_2$ phase (Figure S5); A comparison of the interatomic distances in $Na_3(VO)Fe(PO_4)_2F_2$ obtained from Rietveld refinements by considering two structural descriptions: *Amam* and $P4_2/mnm$ space groups (Table S1); Calculated Fourier difference maps with the residual charge density ranging from 0 - 3 (Figure S6); Calculated Fourier difference maps with the residual charge density ranging from 0 - 1 (Figure S7); Room temperature ^{57}Fe Mössbauer spectra recorded on $Na_3(VO)Fe(PO_4)_2F_2$ and on the charged/discharged sample (Figure S8); Refined room temperature ^{57}Fe Mössbauer hyperfine parameters for $Na_3(VO)Fe(PO_4)_2F_2$ and for the charged/discharged sample (Table S2); Comparison of the cell parameters between the input model and the optimized structure (calculated by GGA method) of $Na_3Fe_2(PO_4)_2F_3$ (Table S3); Electron spin density calculated by GGA method at an iso-surface value of $2 \cdot 10^{-3}$ electron$\cdot$Å^{-1} for $Na_3Fe_2(PO_4)_2F_3$ (Figure S9); Refined parameters of ^{31}P solid-state NMR spectrum of $Na_3(VO)Fe(PO_4)_2F_2$ (Table S4); Comparison of the electrochemical properties between $Na_3(VO)_2(PO_4)_2F$ and $Na_3(VO)Fe(PO_4)_2F_2$ (Figure S10); Comparison of the primary particles' size between $Na_3(VO)_2(PO_4)_2F$ and $Na_3(VO)Fe(PO_4)_2F_2$ (Figure S11); Electrochemical profile of Na//$Na_3(VO)Fe(PO_4)_2F_2$ half-cell used in the operando synchrotron XRD experiment (Figure S12); Le Bail fit of $Na_{2.54}(VO)Fe(PO_4)_2F_2$ (Figure S13); Electrochemical profile of Na//$Na_3(VO)Fe(PO_4)_2F_2$ half-cell used in the operando synchrotron X-ray absorption

experiment (Figure S14); Evolution the absorption edge energy (taken at the normalized intensity = 0.8) of the Vanadium K-edge XANES spectra of $Na_3(VO)Fe(PO_4)_2F_2$ recorded in *operando* condition (Figure S15); Comparing the Vanadium K-edge XANES spectra recorded on a Na//$Na_3(VO)Fe(PO_4)_2F_2$ half-cell in the initial state and at the end of charge (Figure S16); Principal Component Analysis of the Vanadium K-edge XANES spectra recorded in *operando* condition (Figure S17).

References

(1) Larcher, D.; Tarascon, J.-M. Towards Greener and More Sustainable Batteries for Electrical Energy Storage. *Nat. Chem.* **2015**, *7* (1), 19–29. DOI: 10.1038/nchem.2085.

(2) Grey, C. P.; Tarascon, J. M. Sustainability and in Situ Monitoring in Battery Development. *Nat. Mater.* **2016**, *16* (1), 45–56. DOI: 10.1038/nmat4777.

(3) Tarascon, J. M.; Armand, M. Issues and Challenges Facing Rechargeable Lithium Batteries. *Nature* **2001**, *414* (6861), 359–367. DOI: 10.1038/35104644.

(4) Choi, J. W.; Aurbach, D. Promise and Reality of Post-Lithium-Ion Batteries with High Energy Densities. *Nat. Rev. Mater.* **2016**, *1*, 16013(1)-16013(16). DOI: 10.1038/natrevmats.2016.13.

(5) Delmas, C.; Braconnier, J.-J.; Fouassier, C.; Hagenmuller, P. Electrochemical Intercalation of Sodium in Na_xCO_2 Bronzes. *Solid State Ionics* **1981**, *3–4*, 165–169. DOI: 10.1016/0167-2738(81)90076-X.

(6) Park, Y. U.; Seo, D. H.; Kim, H.; Kim, J.; Lee, S.; Kim, B.; Kang, K. A Family of High-Performance Cathode Materials for Na-Ion Batteries, $Na_3(VO_{1-x}PO_4)_2F_{1+2x}$ $(0 \leq x \leq 1)$: Combined First-Principles and Experimental Study. *Adv. Funct. Mater.* **2014**, *24* (29), 4603–4614. DOI: 10.1002/adfm.201400561.

(7) Oh, S. M.; Myung, S. T.; Hassoun, J.; Scrosati, B.; Sun, Y. K. Reversible $NaFePO_4$ Electrode for Sodium Secondary Batteries. *Electrochem. commun.* **2012**, *22* (1), 149–152. DOI: 10.1016/j.elecom.2012.06.014.

(8) Bianchini, M.; Brisset, N.; Fauth, F.; Weill, F.; Elkaim, E.; Suard, E.; Masquelier, C.; Croguennec, L. $Na_3V_2(PO_4)_2F_3$ Revisited: A High-Resolution Diffraction Study. *Chem. Mater.* **2014**, *26* (14), 4238–4247. DOI: 10.1021/cm501644g.

(9) Sharma, N.; Serras, P.; Palomares, V.; Brand, H. E. A.; Alonso, J.; Kubiak, P.; Fdez-gubieda, M. L.; Rojo, T. Sodium Distribution and Reaction Mechanisms of a $Na_3V_2O_2(PO_4)_2F$ Electrode during Use in a Sodium-Ion Battery. *Chem. Mater.* **2014**, *26*, 3391–3402. DOI: 10.1021/cm5005104.

(10) Sauvage, F.; Quarez, E.; Tarascon, J. M.; Baudrin, E. Crystal Structure and Electrochemical Properties vs. Na^+ of the Sodium Fluorophosphate $Na_{1.5}VOPO_4F_{0.5}$. *Solid State Sci.* **2006**, *8* (10), 1215–1221. DOI: 10.1016/j.solidstatesciences.2006.05.009.

(11) Zhou, W.; Xue, L.; Lü, X.; Gao, H.; Li, Y.; Xin, S.; Fu, G.; Cui, Z.; Zhu, Y.; Goodenough, J. B. $Na_xMV(PO_4)_3$ (M = Mn, Fe, Ni) Structure and Properties for Sodium Extraction. *Nano Lett.* **2016**, *16* (12), 7836–7841. DOI: 10.1021/acs.nanolett.6b04044.

(12) Chen, F.; Kovrugin, V. M.; David, R.; Mentré, O.; Fauth, F.; Chotard, J.; Masquelier, C. A NASICON-Type Positive Electrode for Na Batteries with High Energy Density: $Na_4MnV(PO_4)3$. *Small Methods* **2019**, *3*, 1800218(1)–1800218(9). DOI: 10.1002/smtd.201800218.

(13) Abakumov, A. M.; Zakharkin, M. V.; Drozhzhin, O. A.; Antipov, E. V.; Chernyshov, D.; Tereshchenko, I. V.; Stevenson, K. J. Enhancing Na^+ Extraction Limit through High Voltage Activation of the NASICON-Type $Na_4MnV(PO_4)_3$ Cathode. *ACS Appl. Energy Mater.* **2018**, *1* (11), 5842–5846. DOI: 10.1021/acsaem.8b01269.

(14) Guo, J.-Z.; Wang, P.-F.; Wu, X.-L.; Zhang, X.-H.; Yan, Q.; Chen, H.; Zhang, J.-P.; Guo, Y.-G. High-Energy/Power and Low-Temperature Cathode for Sodium-Ion Batteries: In Situ XRD Study and Superior Full-Cell Performance. *Adv. Mater.* **2017**, *29*, 1701968(1)-1701968(8). DOI: 10.1002/adma.201701968.

(15) Gu, Z. Y.; Guo, J. Z.; Yang, Y.; Yu, H. Y.; Xi, X. T.; Zhao, X. X.; Guan, H. Y.; He, X.; Wu, X. L. Precisely Controlled Preparation of an Advanced $Na_3V_2(PO_4)_2O_2F$ Cathode Material for Sodium Ion Batteries: The Optimization of Electrochemical Properties and Electrode Kinetics. *Inorg. Chem. Front.* **2019**, *6* (4), 988–995. DOI: 10.1039/c8qi01374h.

(16) Broux, T.; Fauth, F.; Hall, N.; Chatillon, Y.; Bianchini, M.; Bamine, T.; Leriche, J.; Suard, E.; Carlier, D.; Reynier, Y.; Simonin, L.; Masquelier, C.; Croguennec, L. High Rate Performance for Carbon-Coated $Na_3V_2(PO_4)_2F_3$ in Na-Ion Batteries. *Small Methods* **2019**, *3*, 1800215(1)–1800215(12). DOI: 10.1002/smtd.201800215.

(17) Serras, P.; Palomares, V.; Goñi, A.; Gil de Muro, I.; Kubiak, P.; Lezama, L.; Rojo, T. High Voltage Cathode Materials for Na-Ion Batteries of General Formula $Na_3V_2O_{2x}(PO_4)_2F_{3-2x}$. *J. Mater. Chem.* **2012**, *22* (41), 22301-22308. DOI: 10.1039/c2jm35293a.

(18) Park, Y.; Seo, D.; Kwon, H.; Kim, B.; Kim, J.; Kim, H.; Kim, I.; Yoo, H.; Kang, K. A New High-Energy Cathode for a Na-Ion Battery with Ultrahigh Stability. *J. Am. Chem. Soc.* **2013**, *135*, 13870–13878. DOI: 10.1021/ja406016j.

(19) Xu, M.; Xiao, P.; Stauffer, S.; Song, J.; Henkelman, G.; Goodenough, J. B. Theoretical and Experimental Study of Vanadium-Based Fluorophosphate Cathodes for Rechargeable Batteries. *Chem. Mater.* **2014**, *26* (10), 3089–3097. DOI: 10.1021/cm500106w.

(20) Park, Y. U.; Bai, J.; Wang, L.; Yoon, G.; Zhang, W.; Kim, H.; Lee, S.; Kim, S. W.; Looney, J. P.; Kang, K.; Wang, F. In Situ Tracking Kinetic Pathways of Li^+/Na^+ Substitution during Ion-Exchange Synthesis of $Li_xNa_{1.5-x}VOPO_4F_{0.5}$. *J. Am. Chem. Soc.* **2017**, *139* (36), 12504–12516. DOI: 10.1021/jacs.7b05302.

(21) Bianchini, M.; Lalère, F.; Nguyen, H. B. L.; Fauth, F.; David, R.; Suard, E.; Croguennec, L.; Masquelier, C. $Ag_3V_2(PO_4)_2F_3$, a New Compound Obtained by Ag^+/Na^+ Ion Exchange into the $Na_3V_2(PO_4)_2F_3$ Framework. *J. Mater. Chem. A* **2018**, *6* (22), 10340–10347. DOI: 10.1039/c8ta01095a.

(22) Lin, X.; Huang, J.; Tan, H.; Huang, J.; Zhang, B. $K_3V_2(PO_4)_2F_3$ as a Robust Cathode for Potassium-Ion Batteries. *Energy Storage Mater.* **2019**, *16*, 97–101. DOI: 10.1016/j.ensm.2018.04.026.

(23) Broux, T.; Bamine, T.; Fauth, F.; Simonelli, L.; Olszewski, W.; Marini, C.; Ménétrier, M.; Carlier, D.; Masquelier, C.; Croguennec, L. Strong Impact of the Oxygen Content in $Na_3V_2(PO_4)_2F_{3-y}O_y$ ($0 \le y \le 0.5$) on Its Structural and Electrochemical Properties. *Chem. Mater.* **2016**, *28* (21), 7683–7692. DOI: 10.1021/acs.chemmater.6b02659.

(24) Nguyen, L. H. B.; Broux, T.; Camacho, P. S.; Denux, D.; Bourgeois, L.; Belin, S.; Iadecola, A.; Fauth, F.; Carlier, D.; Olchowka, J.; Masquelier, C.; Croguennec, L. Stability in Water and Electrochemical Properties of the $Na_3V_2(PO_4)_2F_3$ – $Na_3(VO)_2(PO_4)_2F$ Solid Solution. *Energy Storage Mater.* **2019**, *20*, 324–334. DOI: 10.1016/j.ensm.2019.04.010.

(25) Bianchini, M.; Xiao, P.; Wang, Y.; Ceder, G. Additional Sodium Insertion into Polyanionic Cathodes for Higher-Energy Na-Ion Batteries. *Adv. Energy Mater.* **2017**, *7* (18), 1700514(1) - 1700514(9). DOI: 10.1002/aenm.201700514.

(26) Olchowka, J.; Nguyen, L. H. B.; Broux, T.; Sanz Camacho, P.; Petit, E.; Fauth, F.; Dany, C.; Masquelier, C.; Croguennec, L. Aluminum Substitution for Vanadium in the $Na_3V_2(PO_4)_2F_3$ and $Na_3V_2(PO_4)_2FO_2$ Type Materials. *Chem. Commun.* **2019**. Accepted. DOI: 10.1039/C9CC05137F.

(27) Liu, W.; Yi, H.; Zheng, Q.; Li, X.; Zhang, H. Y-Doped $Na_3V_2(PO_4)_2F_3$ Compounds for Sodium Ion Battery Cathodes: Electrochemical Performance and Analysis of Kinetic Properties. *J. Mater. Chem. A* **2017**, *5* (22), 10928–10935. DOI: 10.1039/C7TA03133E.

(28) Zhang, Y.; Guo, S.; Xu, H. Synthesis of Uniform Hierarchical $Na_3V_{1.95}Mn_{0.05}(PO_4)_2F_3$@C Hollow Microspheres as a Cathode Material for Sodium-Ion Batteries. *J. Mater. Chem. A* **2018**, *6* (10), 4525–4534. DOI: 10.1039/C7TA11105C.

(29) Qi, Y.; Mu, L.; Zhao, J.; Hu, Y.; Liu, H.; Dai, S. Superior Na-Storage Performance of Low-Temperature-Synthesized $Na_3(VO_{1-x}PO_4)_2F_{1+2x}$ $(0 \leq x \leq 1)$ Nanoparticles for Na-Ion Batteries. *Angew. Chemie* **2015**, *127* (34), 10049–10054. DOI: 10.1002/ange.201503188.

(30) Rodríguez-Carvajal, J. Recent Advances in Magnetic Structure Determination by Neutron Powder Diffraction. *Phys. B Condens. Matter* **1993**, *192*, 55–69. DOI: 10.1016/0921-4526(93)90108-I.

(31) Petříček, V.; Dušek, M.; Palatinus, L. Crystallographic Computing System JANA2006 : General Features. *Z. Krist.* **2014**, *229* (5), 345–352. DOI: 10.1515/zkri-2014-1737.

(32) Momma, K.; Izumi, F. VESTA: A Three-Dimensional Visualization System for Electronic and Structural Analysis. *J. Appl. Crystallogr.* **2008**, *41* (3), 653–658. DOI: 10.1107/S0021889808012016.

(33) Leriche, J. B.; Hamelet, S.; Shu, J.; Morcrette, M.; Masquelier, C.; Ouvrard, G.; Zerrouki, M.; Soudan, P.; Belin, S.; Elkaïm, E.; Baudelet, F. An Electrochemical Cell for Operando Study of Lithium Batteries Using Synchrotron Radiation. *J. Electrochem. Soc.* **2010**, *157* (5), A606-A610. DOI: 10.1149/1.3355977.

(34) Hesse, J.; Rubartsch, A. Model Independent Evaluation of Overlapped Mossbauer Spectra. *J. Phys. E.* **1974**, *7* (7), 526–532. DOI: 10.1088/0022-3735/7/7/012.

(35) Briois, V.; La Fontaine, C.; Belin, S.; Barthe, L.; Moreno, T.; Pinty, V.; Carcy, A.; Girardot, R.; Fonda, E. ROCK: The New Quick-EXAFS Beamline at SOLEIL. *J. Phys. Conf. Ser.* **2016**, *712*, 1-6. DOI: 10.1088/1742-6596/712/1/012149.

(36) Fonda, E.; Rochet, A.; Ribbens, M.; Barthe, L.; Belin, S.; Briois, V. The SAMBA Quick-EXAFS Monochromator: XAS with Edge Jumping. *J. Synchrotron Radiat.* **2012**, *19* (3), 417–424. DOI: 10.1107/S0909049512009703.

(37) Lesage, C.; Devers, E.; Legens, C.; Fernandes, G.; Roudenko, O.; Briois, V. High Pressure Cell for Edge Jumping X-Ray Absorption Spectroscopy: Applications to Industrial Liquid Sulfidation of Hydrotreatment Catalysts. *Catal. Today* **2019**, *336*, 63–73. DOI: 10.1016/j.cattod.2019.01.081.

(38) Ravel, B.; Newville, M. ATHENA, ARTEMIS, HEPHAESTUS: Data Analysis for X-Ray Absorption Spectroscopy Using IFEFFIT. *J. Synchrotron Radiat.* **2005**, *12* (4), 537–

541. DOI: 10.1107/S0909049505012719.

(39) Nguyen, L. H. B.; Sanz Camacho, P.; Broux, T.; Masquelier, C.; Croguennec, L.; Carlier, D. ^{23}Na and ^{31}P Solid-State NMR: A Key Tool to Study Local Environments in $Na_3V_2(PO_4)_2F_{3-y}O_y$ ($0 \leq y \leq 2$) Materials. *In ECS 235th meeting*; **2019**, Abstract #544.

(40) Kresse, G.; Furthmüller, J. Efficiency of Ab-Initio Total Energy Calculations for Metals and Semiconductors Using a Plane-Wave Basis Set. *Comput. Mater. Sci.* **1996**, *6* (1), 15–50. DOI: 10.1016/0927-0256(96)00008-0.

(41) Tsirlin, A. A.; Nath, R.; Abakumov, A. M.; Furukawa, Y.; Johnston, D. C.; Hemmida, M.; Krug Von Nidda, H. A.; Loidl, A.; Geibel, C.; Rosner, H. Phase Separation and Frustrated Square Lattice Magnetism of $Na_{1.5}VOPO_4F_{0.5}$. *Phys. Rev. B - Condens. Matter Mater. Phys.* **2011**, *84* (1), 2–13. DOI: 10.1103/PhysRevB.84.014429.

(42) Le Meins, J.-M.; Crosnier-Lopez, M.-P.; Hemon-Ribaud, A.; Courbion, G. Phase Transitions in the $Na_3M_2(PO_4)_2F_3$ Family (M = Al^{3+}, V^{3+}, Cr^{3+}, Fe^{3+}, Ga^{3+}): Synthesis, Thermal, Structural, and Magnetic Studies. *J. Solid State Chem.* **1999**, *148*, 260–277. DOI: 10.1006/jssc.1999.8447.

(43) Bill, E. ^{57}Fe-Mössbauer Spectroscopy and Basic Interpretation of Mössbauer Parameters. In *Practical Approaches to Biological Inorganic Chemistry*; Elsevier, 2013; 109–130. DOI: 10.1016/B978-0-444-56351-4.00005-1.

(44) Penner-Hahn, J. E. X-Ray Absorption Spectroscopy. In *Comprehensive Coordination Chemistry II*; Elsevier, 2003; 159–186. DOI: 10.1016/B0-08-043748-6/01063-X.

(45) Dacek, S. T.; Richards, W. D.; Kitchaev, D. A.; Ceder, G. Structure and Dynamics of Fluorophosphate Na-Ion Battery Cathodes. *Chem. Mater.* **2016**, *28* (15), 5450–5460. DOI: 10.1021/acs.chemmater.6b01989.

(46) Matts, I. L.; Dacek, S.; Pietrzak, T. K.; Malik, R.; Ceder, G. Explaining Performance-Limiting Mechanisms in Fluorophosphate Na-Ion Battery Cathodes through Inactive Transition-Metal Mixing and First-Principles Mobility Calculations. *Chem. Mater.* **2015**, *27* (17), 6008–6015. DOI: 10.1021/acs.chemmater.5b02299.

(47) Chihara, K.; Kitajou, A.; Gocheva, I. D.; Okada, S.; Yamaki, J. I. Cathode Properties of $Na_3M_2(PO_4)_2F_3$[M = Ti, Fe, V] for Sodium-Ion Batteries. *J. Power Sources* **2013**, *227*, 80–85. DOI: 10.1016/j.jpowsour.2012.10.034.

(48) Zhang, B.; Dugas, R.; Rousse, G.; Rozier, P.; Abakumov, A. M.; Tarascon, J.-M. Insertion Compounds and Composites Made by Ball Milling for Advanced Sodium-Ion Batteries. *Nat. Commun.* **2016**, *7* (1), 10308(1)-10308(9). DOI: 10.1038/ncomms10308.

(49) Bianchini, M.; Fauth, F.; Brisset, N.; Weill, F.; Suard, E.; Masquelier, C.; Croguen. Comprehensive Investigation of the $Na_3V_2(PO_4)_2F_3$–$NaV_2(PO_4)_2F_3$ System by Operando High Resolution Synchrotron X-ray Diffraction. *Chem. Mater.* **2015**, *27*, 3009–3020. DOI: 10.1021/acs.chemmater.5b00361.

(50) Massart, D. L.; Vandeginste, B. G. M.; Buydens, L. M. C.; Jong, S. D.; Lewi, P. J.; Smeyers-Verbeke, J. *Handbook of Chemometrics and Qualimetrics: Part A*; Elsevier: Amsterdam, 1997, 1-867.

(51) Garrido, M.; Larrechi, M. S.; Rius, F. X.; Tauler, R. Calculation of Band Boundaries of Feasible Solutions Obtained by Multivariate Curve Resolution–Alternating Least Squares of Multiple Runs of a Reaction Monitored by NIR Spectroscopy. *Chemom.*

Intell. Lab. Syst. **2005**, *76* (2), 111–120. DOI: 10.1016/j.chemolab.2004.10.001.

(52) Jaumot, J.; de Juan, A.; Tauler, R. MCR-ALS GUI 2.0: New Features and Applications. *Chemom. Intell. Lab. Syst.* **2015**, *140*, 1–12. DOI: 10.1016/j.chemolab.2014.10.003.